Supporting Information

Inner space- and architecture-controlled nanoframes for efficient electro-oxidation of liquid fuels

Daowei Gao[a,b,#], Shuna Li[a,#], Guolong Song[a], Mingchuan Luo[c], Yipin Lv[a], Shaohan Yang[a], Xinlong Ma*[d], Xin Zhang[d], Cuncheng Li[a], Qin Wei[a], and Guozhu Chen*[a]*

[a]School of Chemistry and Chemical Engineering, University of Jinan, Jinan 250022, PR China

[b]Helmholtz-Zentrum Berlin für Materialien und Energie GmbH, Berlin 12489, Germany

[c]Department of Materials Science and Engineering, College of Engineering, Peking University, Beijing, 100871, China

[d]State Key Laboratory of Heavy Oil Processing, China University of Petroleum, Beijing 102249, PR China

[#]Daowei Gao and Shuna Li contributed equally to this work.

*To whom correspondence should be addressed:

E-mail: chm_chengz@ujn.edu.cn; mingchuanluo@foxmail.com; maxl@cup.edu.cn

Table S1. Surface composition and oxidation state of PtCuNi NPs from XPS analysis.

Sample	Pt(II)/Pt(0)	Cu(II)/(Cu(I)+ Cu(0))	Ni(II)/Ni(0)
PtCuNi o-NFs	0.52	0.45	2.17
PtCuNi c-NFs	0.86	0.72	2.78
PtCuNi h-NFs	0.89	0.46	0.88
PtCuNi HWs	0.53	0.74	3.97

Table S2. Peak and onset potential of CO stripping on various catalysts.

sample	onset potential of CO oxidation vs SCE (V)	peak potential of CO oxidation vs SCE (V)
PtCuNi c-NFs	0.39	0.52
PtCuNi o-NFs	0.43	0.60
PtCuNi h-NFs	0.59	0.65
PtCuNi HWs	0.61	0.69
PtCuNi th-NFs	0.59	0.64
Pt /C	0.62	0.70

Table S3. Calculated adsorption energies (ΔE) of OH, H and CH_3OH and d-band centers of Pt, Cu, and Ni on different metallic surfaces.

Surfaces	ΔE (eV)			ε_d (eV)		
	OH	H	CH_3OH	Pt	Cu	Ni
Pt(111)	-2.54	-0.39	-0.65	-2.51	--	--
$Pt_1Cu_{5/3}$(111)	-3.57	-0.17	-0.61	-2.24	-2.05	--
$Ni_xPt_1Cu_{5/3}$(111)	-3.68	-0.37	-0.55	-2.29	-2.05	-1.41
$Ni_xPt_1Cu_1$(111)	-3.33	-0.40	-0.52	-2.21	-1.91	-1.17
$Ni_xPt_1Cu_3$(111)	-3.67	-0.44	-0.52	-2.30	-2.07	-1.20
$Ni_xPt_1Cu_{5/3}$(211)	-3.88	-0.29	-0.38	-2.14	-1.87	-0.72

Table S4. Performance comparison of MOR and FAOR over Pt-based catalysts with recent literatures

Catalysts	Specific activity (mA/cm^2)		Mass activity ($mA/\mu g_{Pt}$)		Reference
	CH_3OH	CHOOH	CH_3OH	CHOOH	
PtCuNi c-NFs	5.04	2.39	1.08	0.52	This work
PtCuNi o-NFs	4.68	2.04	0.51	0.23	This work
Pt–Mn–Cu CNC	4.13	1.87	0.42	0.19	[1]
Pt–Cu CNC	4.70	–	–	–	[2]
Pt–Ni HOH	1.70	0.13	0.45	0.07	[3]
Pt–Pd CNC	8.50	–	0.32	–	[4]
Pt–Cu–Ni CNC	1.97	1.50	0.11	0.07	[5]
Pt Concave	–	3.70	–	0.18	[6]
Pt_3V/C	0.38	–	0.20	–	[7]
Pt_3Ti/C	0.31	–	0.15	–	[7]
PtAgCu@PtCu	–	1.63	–	0.31	[8]
Pt–Co NWs	1.95	–	1.02	–	[9]
Pt–Pd Hollow	1.36	–	0.58	–	[10]

Table S5. Comparison of the activity of commercial Pt in the literatures.

Catalysts	Specific activity (mA/cm^2)		References
	CH_3OH	CHOOH	
Pt/C	0.46	0.16	This work
		0.22	[11]
	0.47	0.23	[12]
	0.83	0.62	[13]
	1.19	-	[14]
	0.56	-	[15]
	0.59	-	[16]
	0.46	-	[17]
	0.4		[18]
	0.47	0.23	[19]
	1.04		[20]
	0.35	0.82	[21]
	0.3		[22]
	1.25		[23]

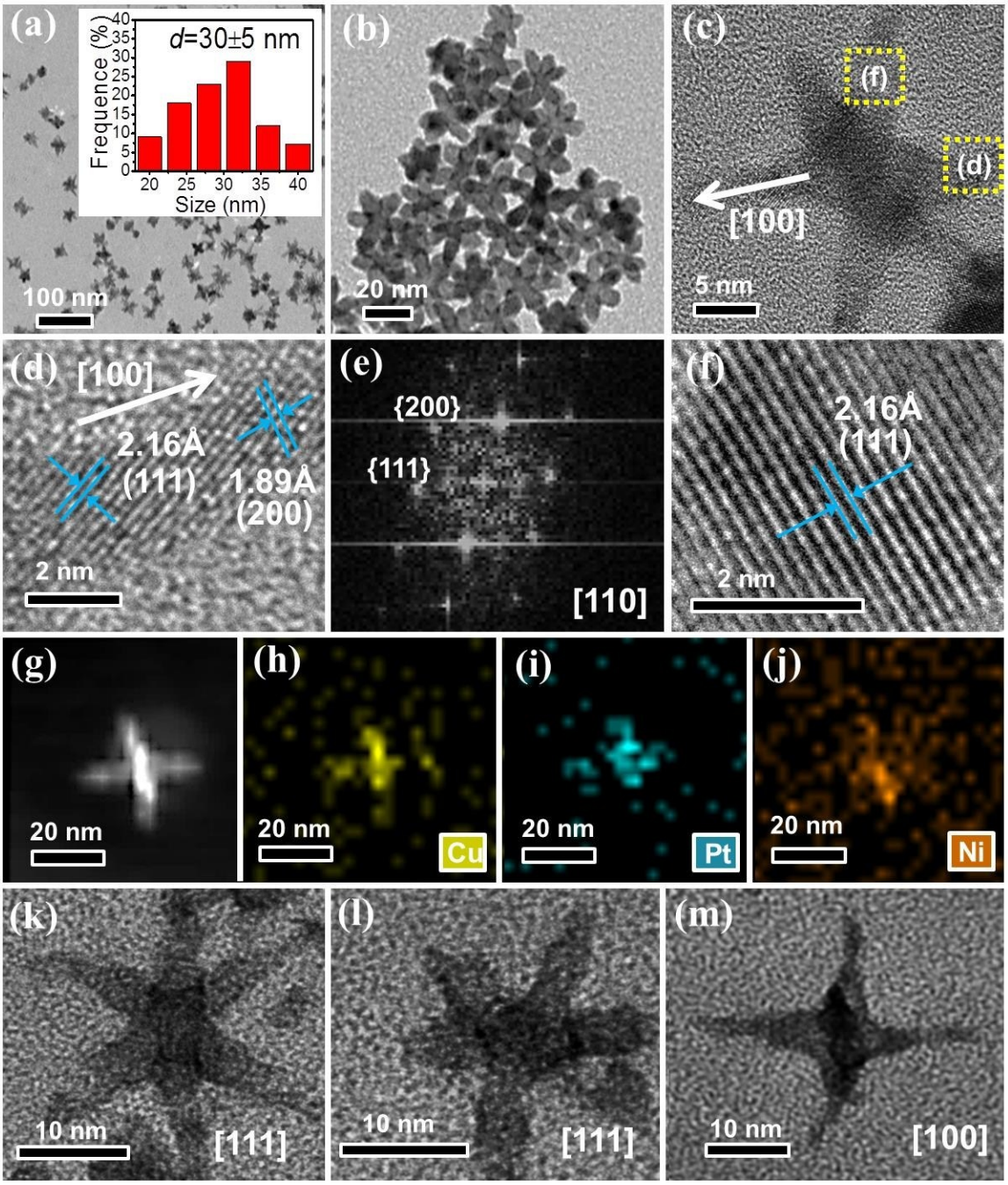

Figure S1. (a–b) TEM, size-distribution histogram (inset), (c–f) HRTEM and FFT images of PtCuNi h-NFs. (g) HAADF-STEM and (h–j) EDS mapping images of PtCuNi h-NFs. (k–m) TEM images and structural models of PtCuNi h-NFs viewed along the (k) [111], (l) [111], and (m) [100] directions.

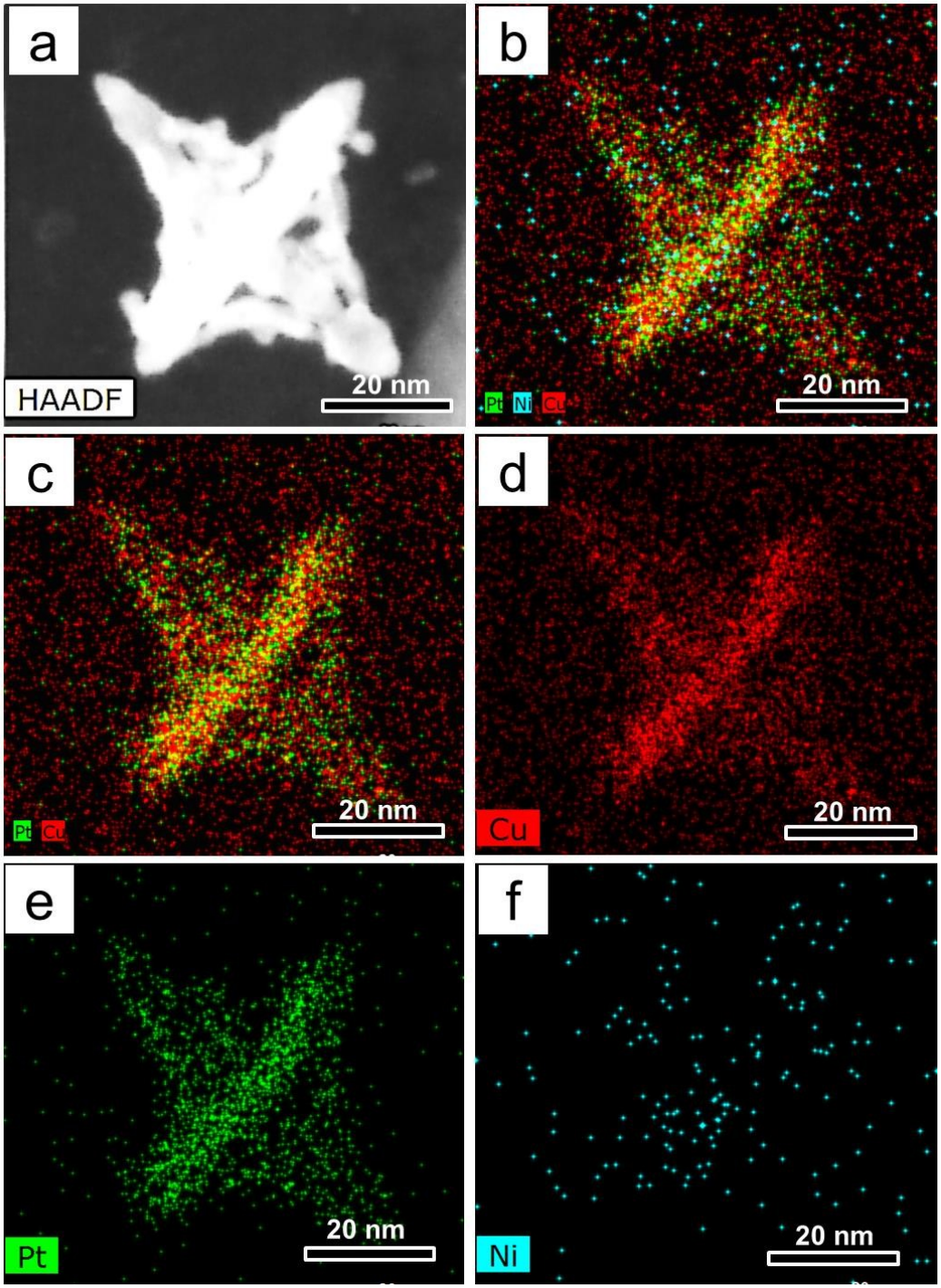

Figure S2. (a) HAADF-STEM and (b-f) EDS-mapping images of PtCuNi o-NFs.

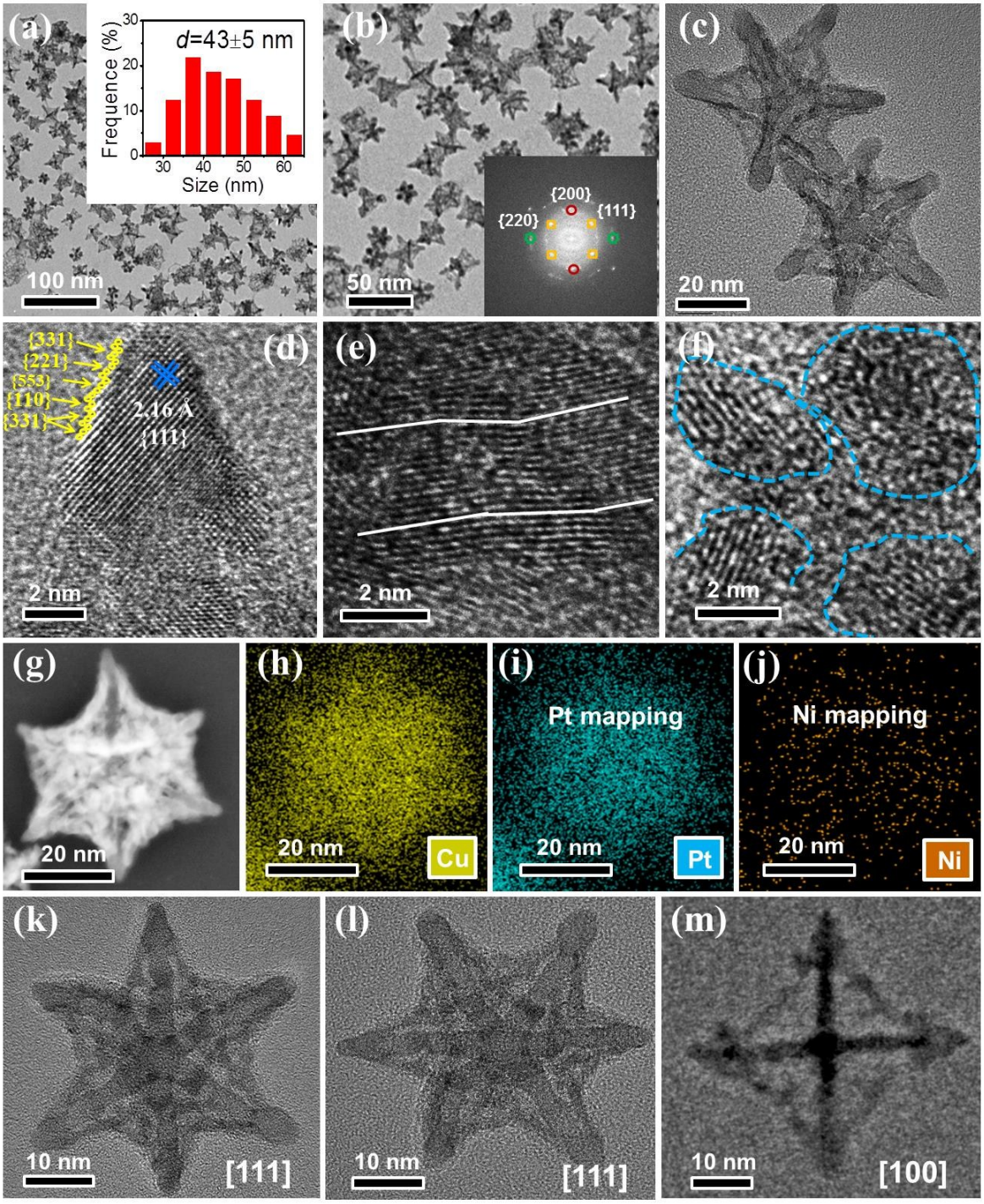

Figure S3. (a–c) TEM, size-distribution histogram (inset), FFT (inset), (d) step atoms, and (e, f) interfacial dislocation images of PtCuNi c-NFs. (g) HAADF-STEM and (h–j) EDS mapping images of PtCuNi c-NFs. (k–m) TEM images and structural models of PtCuNi c-NFs viewed along the (k) [111], (l) [111], and (m) [100] directions.

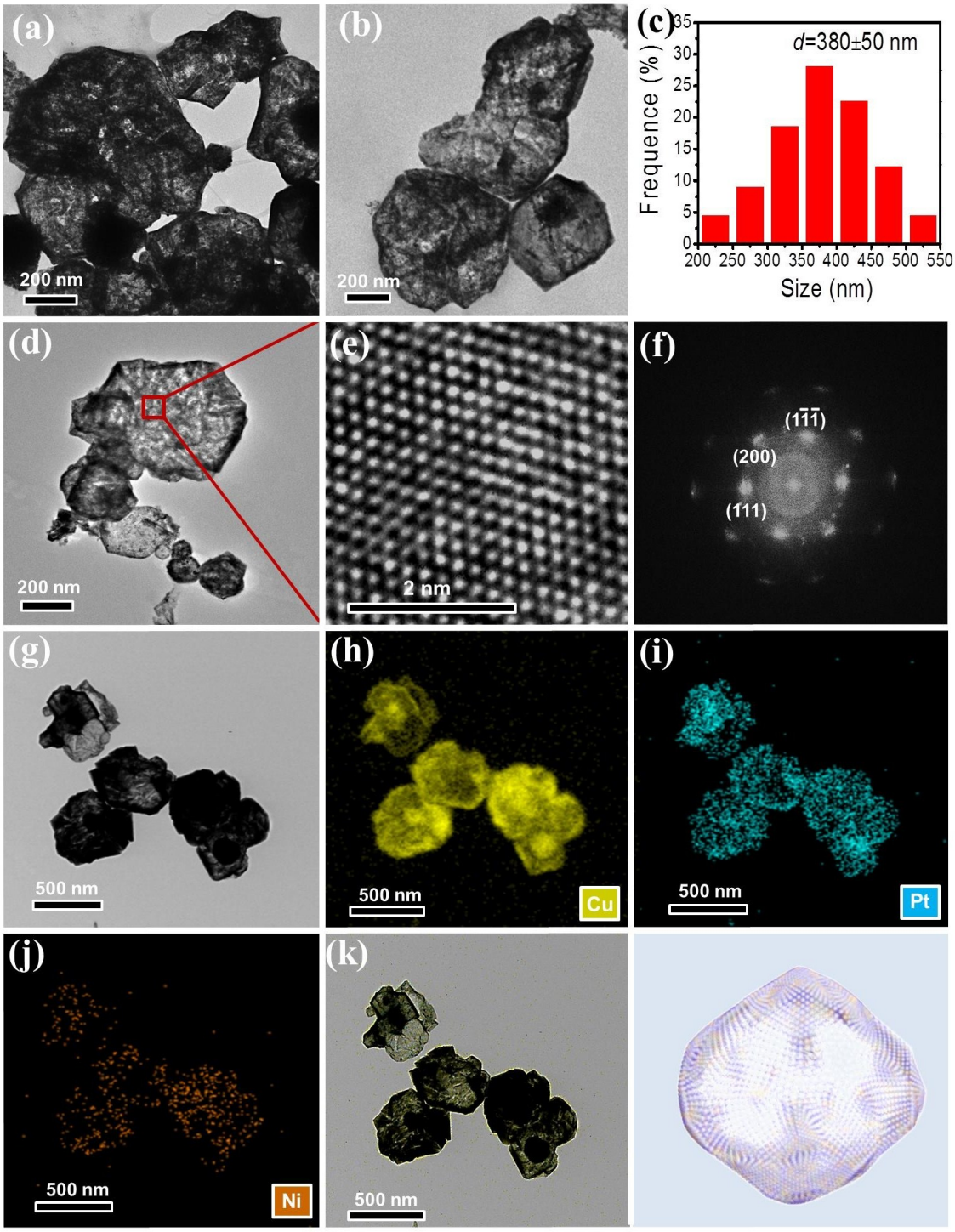

Figure S4. (a-d) TEM images, size-distribution histogram of PtCuNi HWs. (e) The HRTEM, (f) corresponding FFT, and (g-k) EDS-mapping images of PtCuNi HWs.

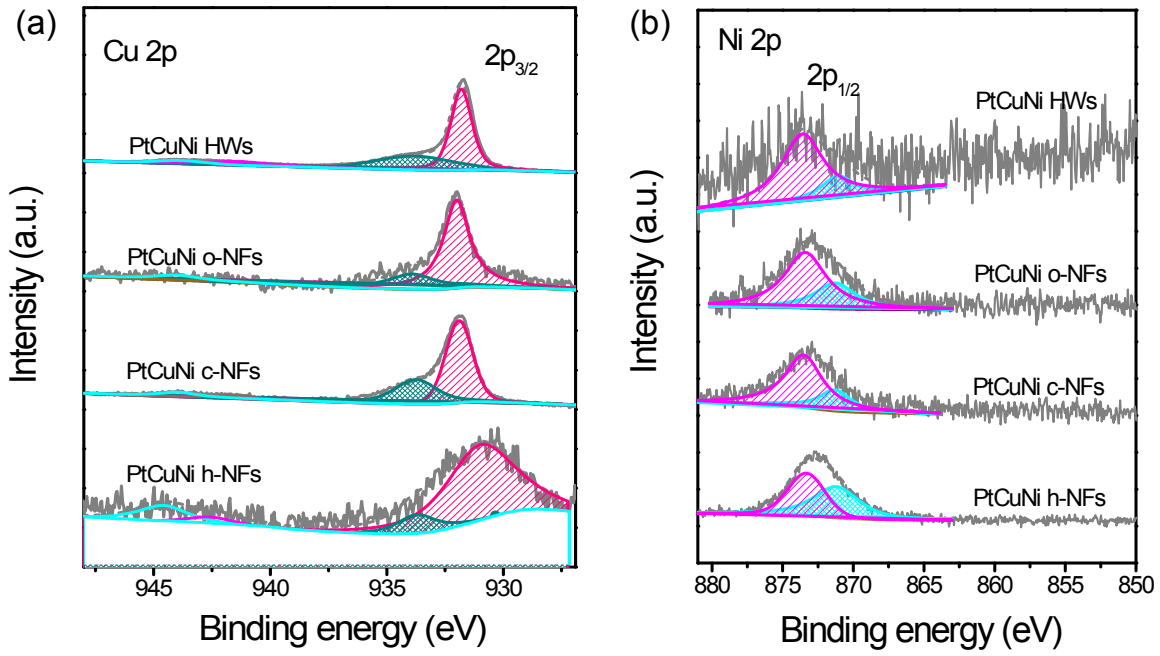

Figure S5. XPS spectra of (a) Cu 2p and (b) Ni 2p for PtCuNi with different structures.

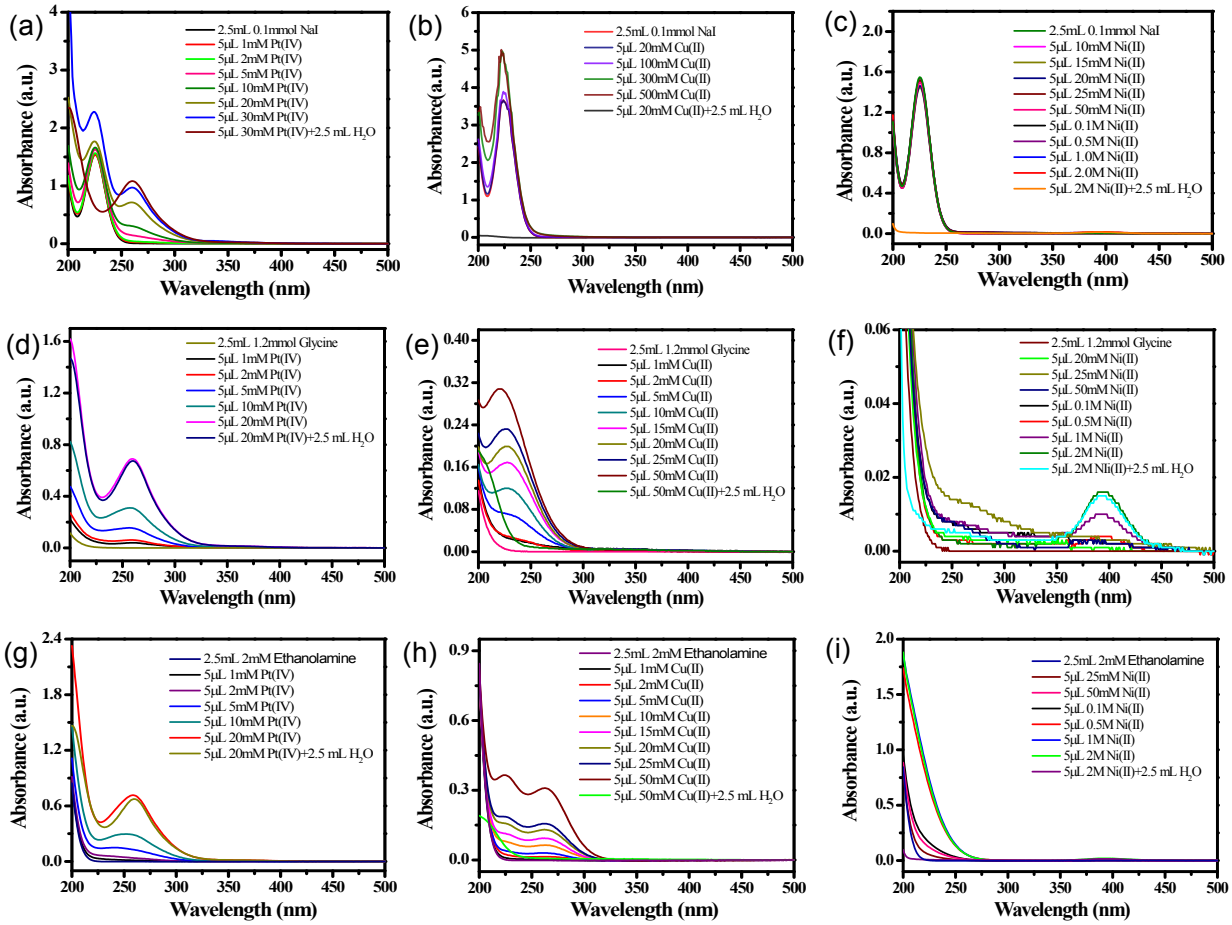

Figure S6. Study of the interaction between (a-c) I⁻, (d-f) glycine and (g-i) ethanolamine and Pt(IV), Cu(II) and Ni(II) ions by UV–vis spectroscopy at room temperature.

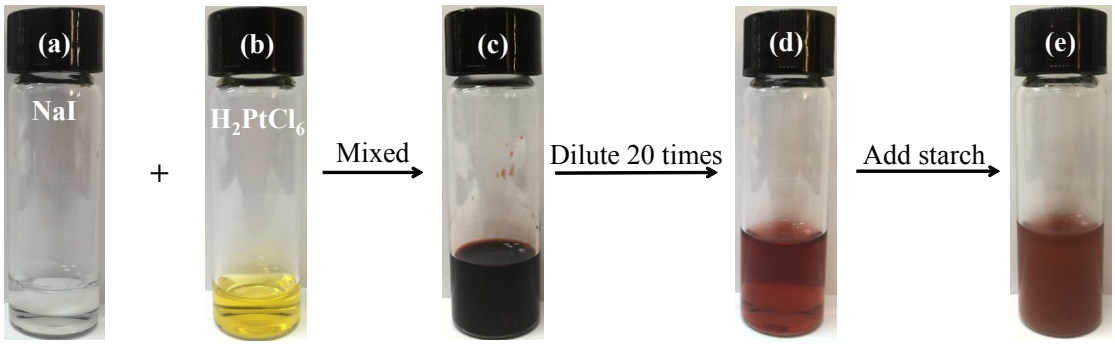

Figure S7. The study of the reaction between H_2PtCl_6 and NaI.

$$PtCl_6^{2-} + 6I^- \rightarrow PtI_6^- + 6Cl^- \qquad \text{(Equation S3)}$$

(the ligand exchange reaction)

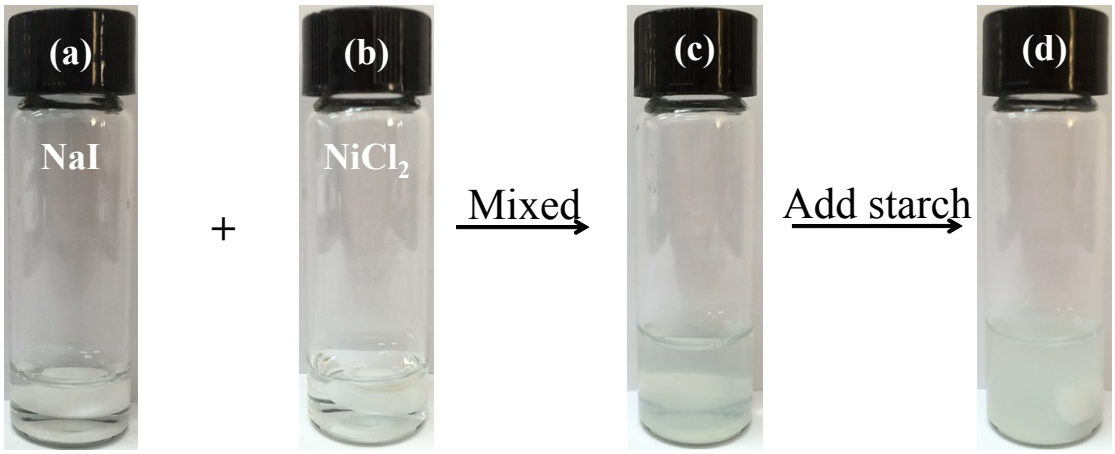

Figure S8. The study of the reaction between $NiCl_2$ and NaI.

The Ni(II) ions has no react with I^-.

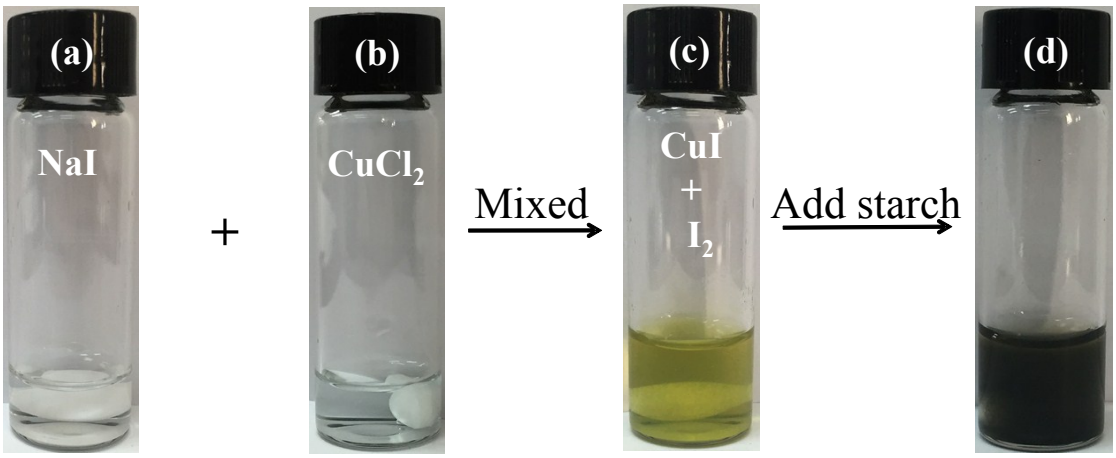

Figure S9. The study of the reaction between Cu(II) and NaI.

$$Cu^{2+} + 2I^{-} \rightarrow CuI_2 \qquad \text{(Equation S4)}$$

$$2CuI_2 \rightarrow 2CuI + I_2 \qquad \text{(Equation S5)}$$

It can be found from the starch reaction that the reaction of Cu^{2+} and I^- produces I_2. According to reference, the reaction of Cu^{2+} and I^- first generates CuI_2. The CuI nanocrystals have poor stability, and further formation of CuI and I_2.

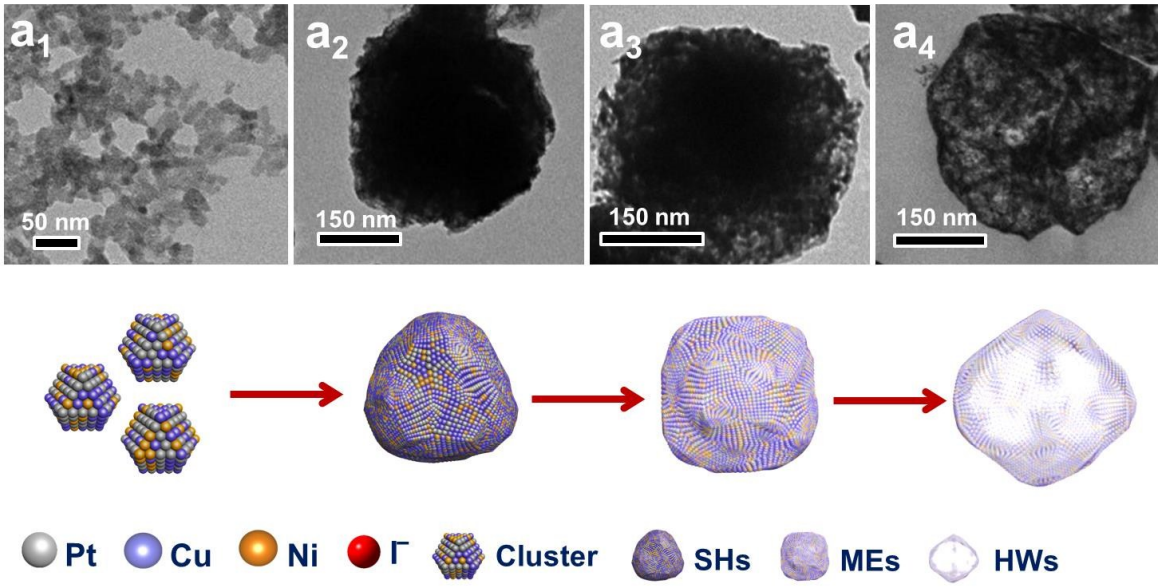

Figure S10. TEM images investigating the course of morphological evolution for PtCuNi with the absence of NaI. (a_1)–(a_4) represent the reaction time at 1, 5, 20, and 30 min, respectively.

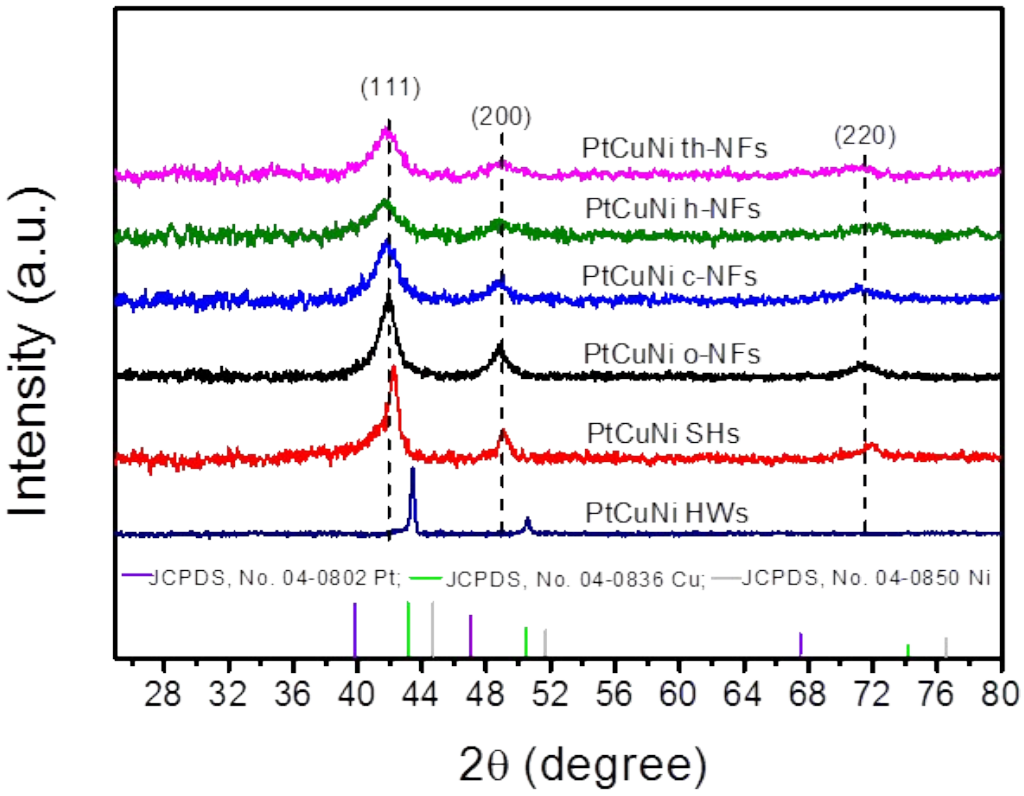

Figure S11. XRD patterns of PtCuNi with different structures.

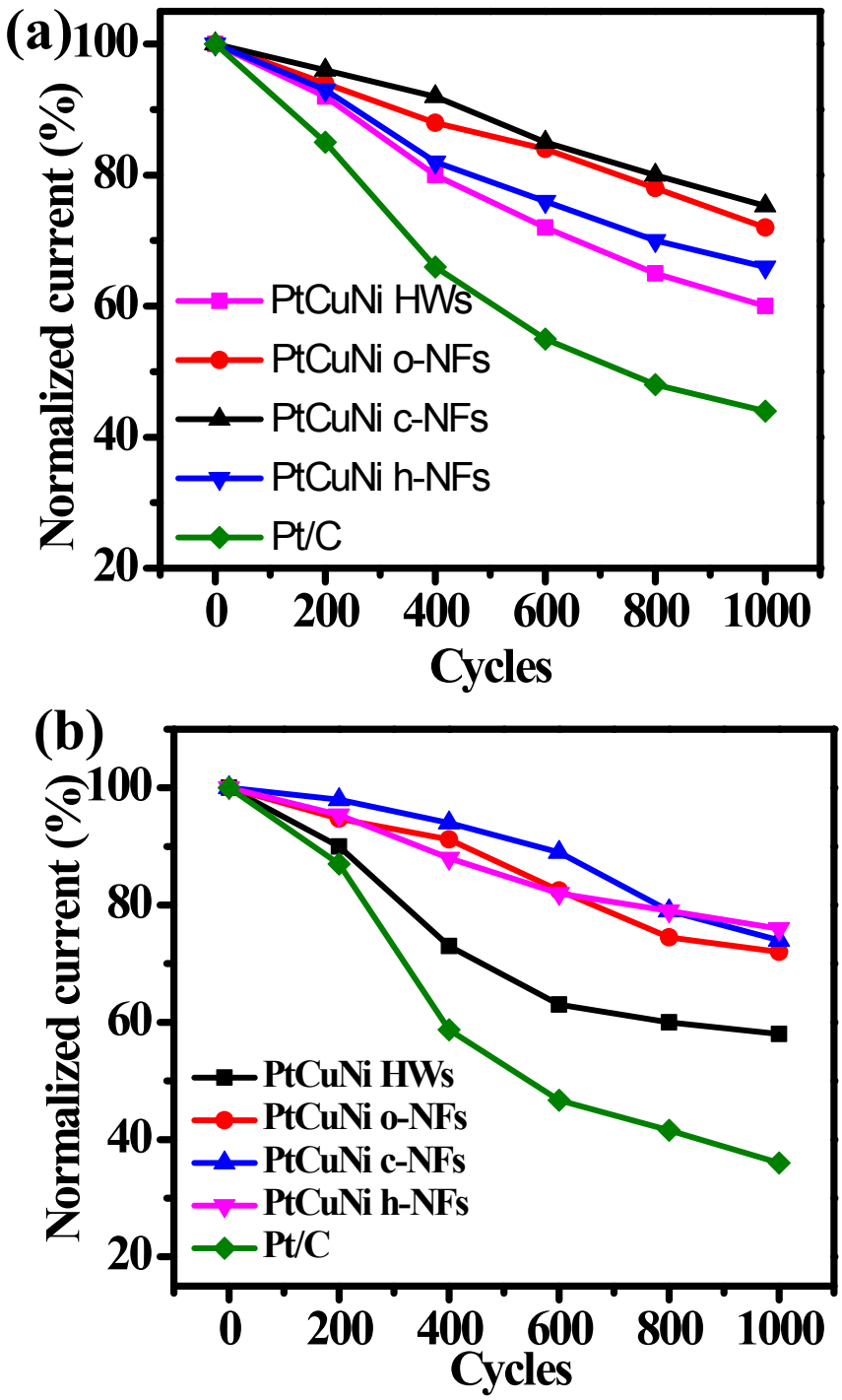

Figure S12. The loss of peak current densities of MOR and FAOR as a function of the number of cycles on different electrocatalysts. The potential was scanned from −0.24 to 1.0 V (vs SCE) with a sweep rate of 50 mV s^{-1}.

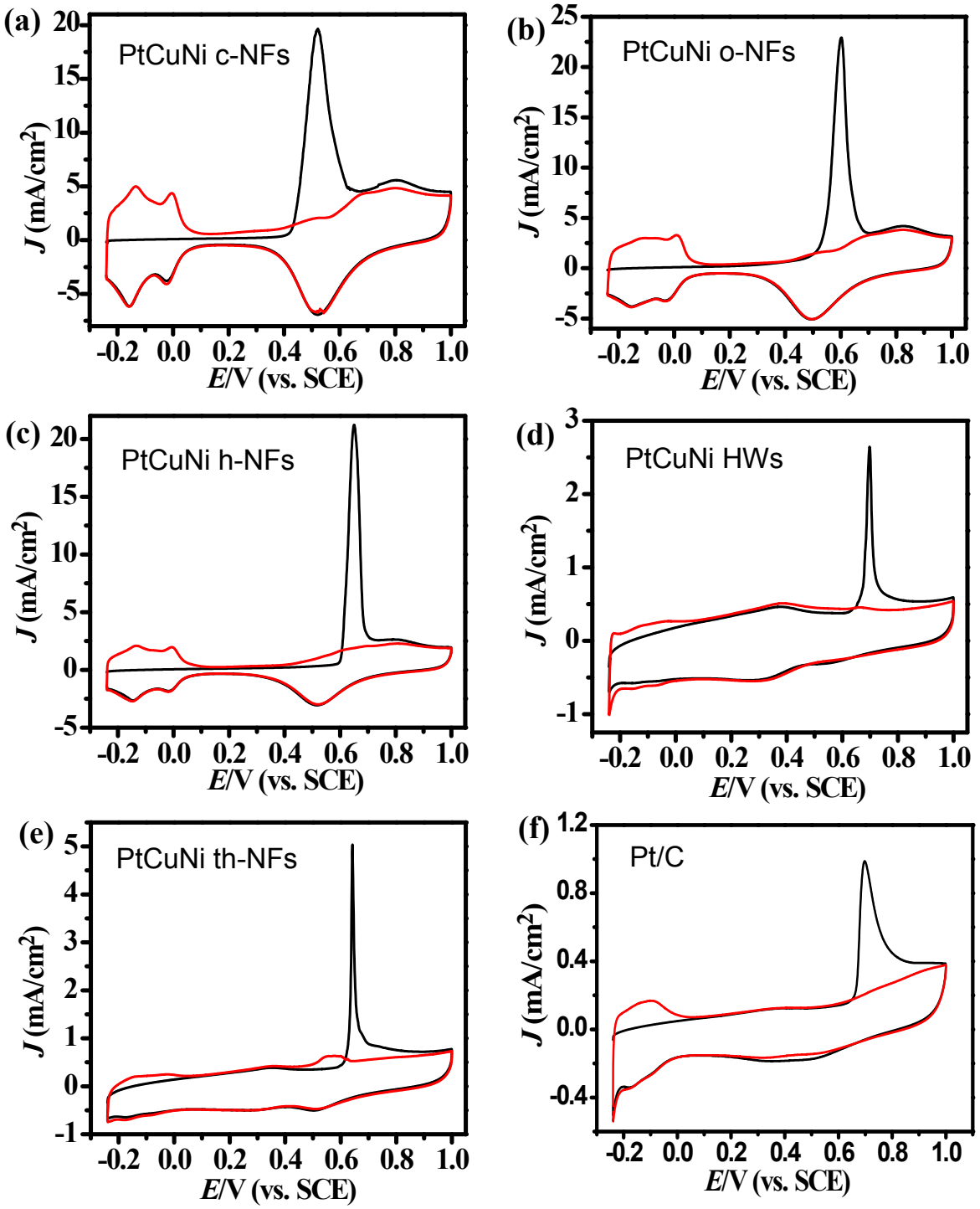

Figure S13. CO-stripping voltammograms (black line standing for first cycle, red line standing for second cycle) of these catalysts in 0.5 M H_2SO_4 at a scan rate of 50 mV/s.

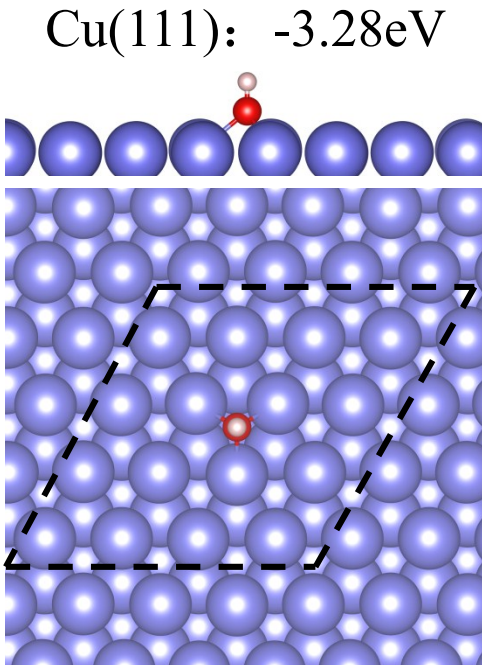

Figure S14. Side (upper panel) and top (lower panel) views of OH adsorption on Cu(111) surfaces, including corresponding adsorption energies. Dashed lines indicate the (4×4) supercell for (111) surfaces.

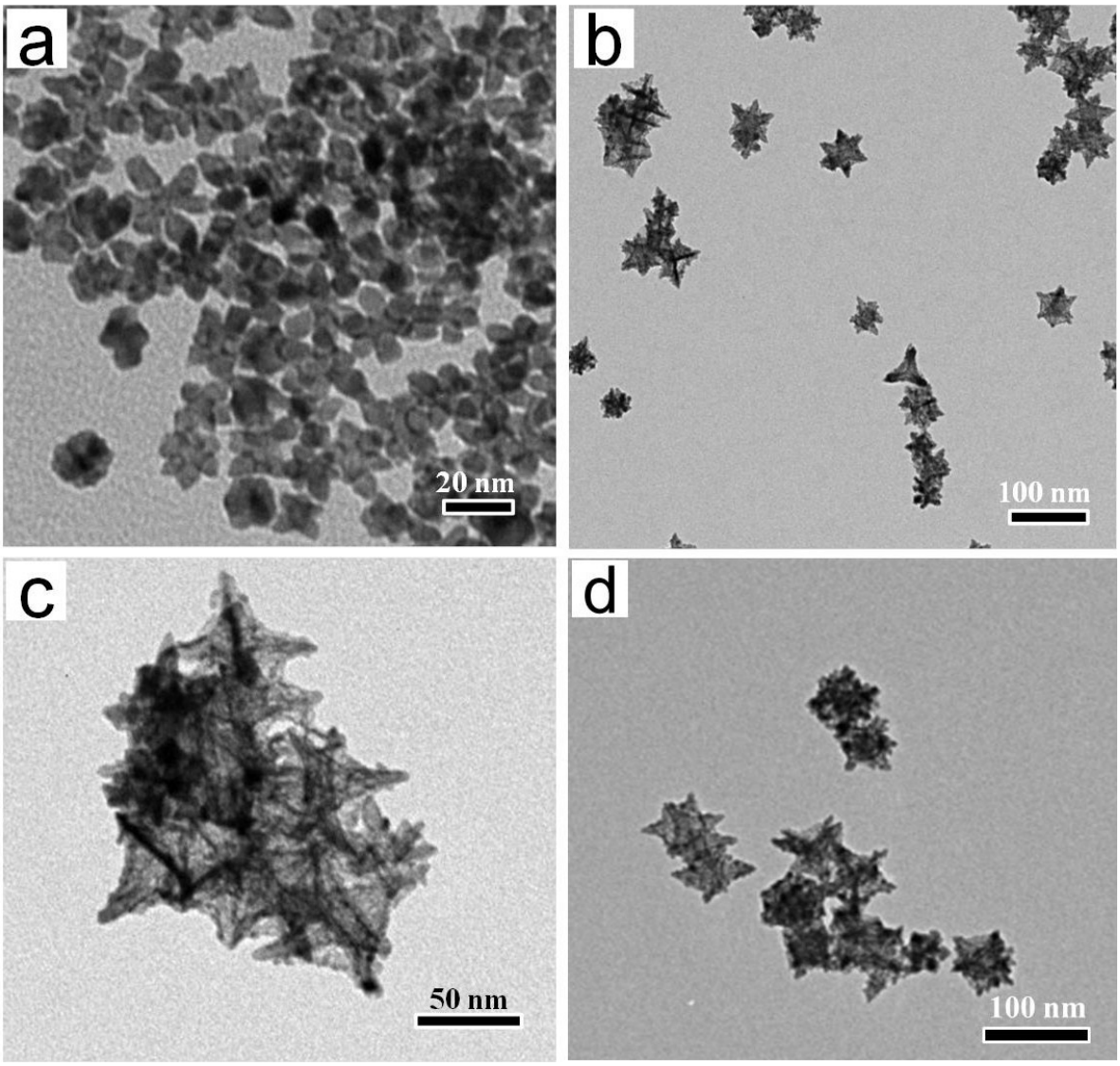

Figure S15. TEM images of PtCuFe, PtCuCo, PtCuMn and PtCuCr alloy NFs synthesized with the similar method.

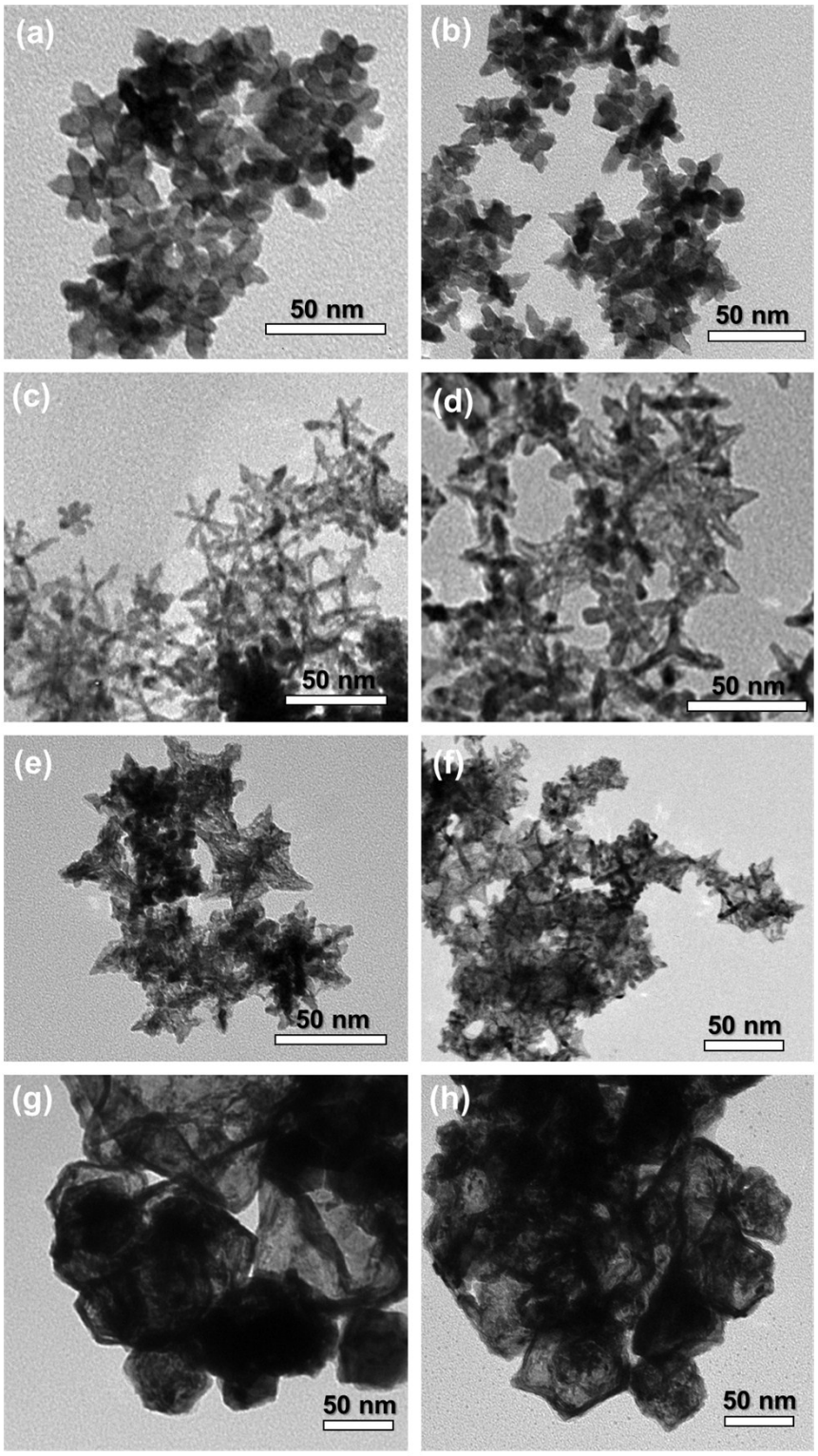

Figure S16. The TEM images of Pt-based alloy after 1000 potential cycles for MOR (a, c, e and g) and FAOR (b, d, f and h). Notes: PtCuNi h-NFs (a and b), PtCuNi o-NFs (c and d), PtCuNi c-NFs (e and f) and PtCuNi HWs (g and h).

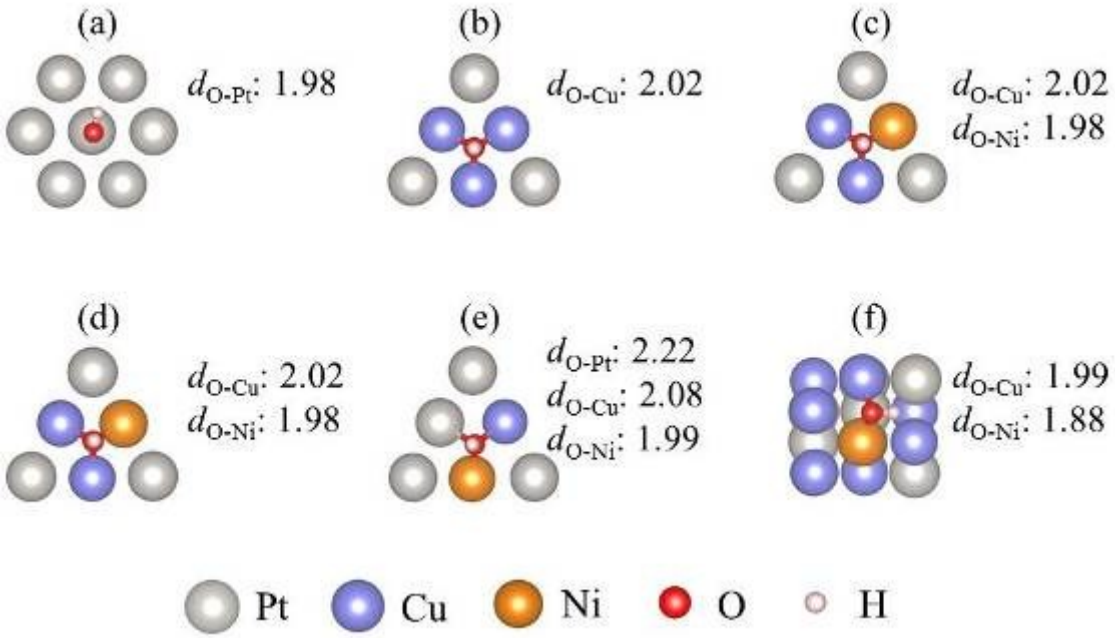

Figure S17. O-metal bond lengths (in Å) of OH adsorption on (a) Pt(111), (b) $Pt_1Cu_{5/3}$(111), (c) $Pt_1Cu_{5/3}Ni_x$ (111), (d) $Pt_1Cu_3Ni_x$ (111), (e) $Pt_1Cu_1Ni_x$ (111) and (d) $Pt_1Cu_{5/3}Ni_x$ (211) surfaces.

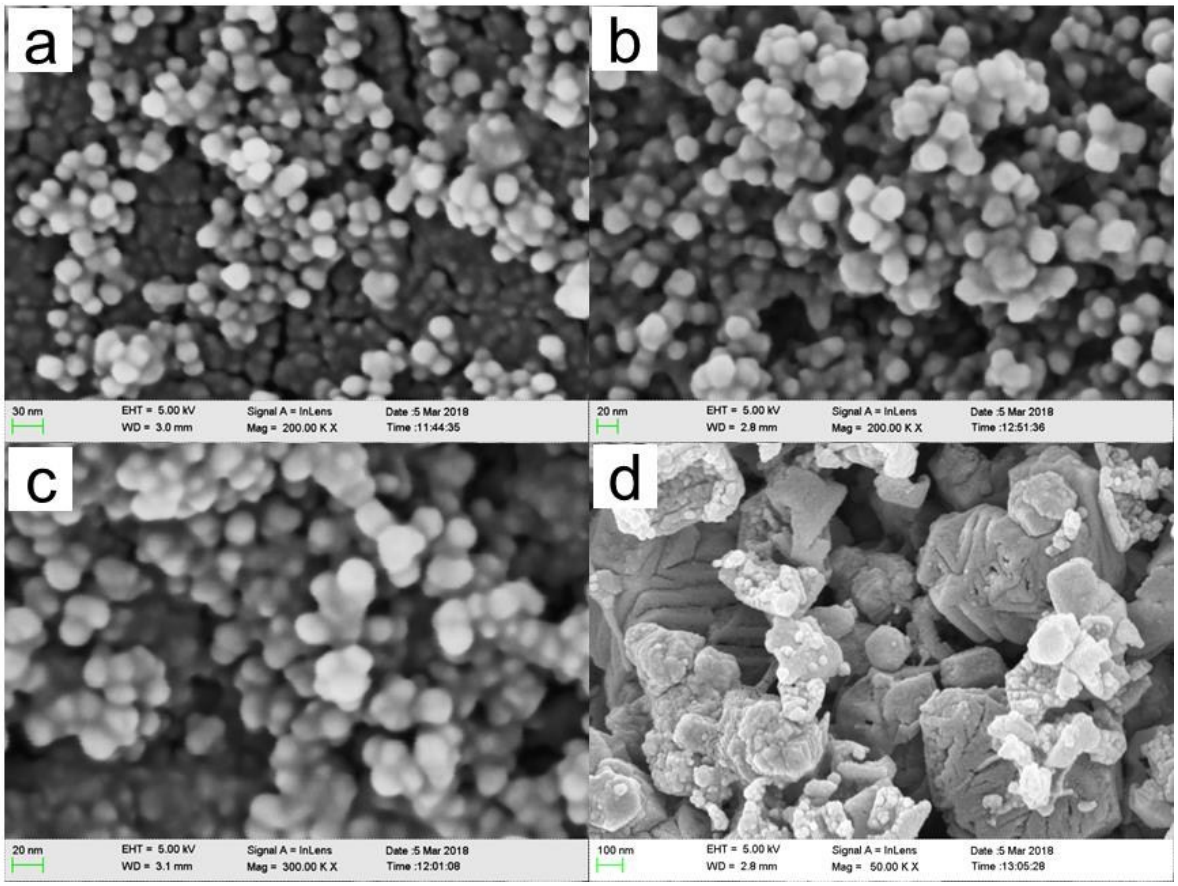

Figure S18. SEM images of h-NFs, o-NFs, c-NFs, and HWs PtCuNi.

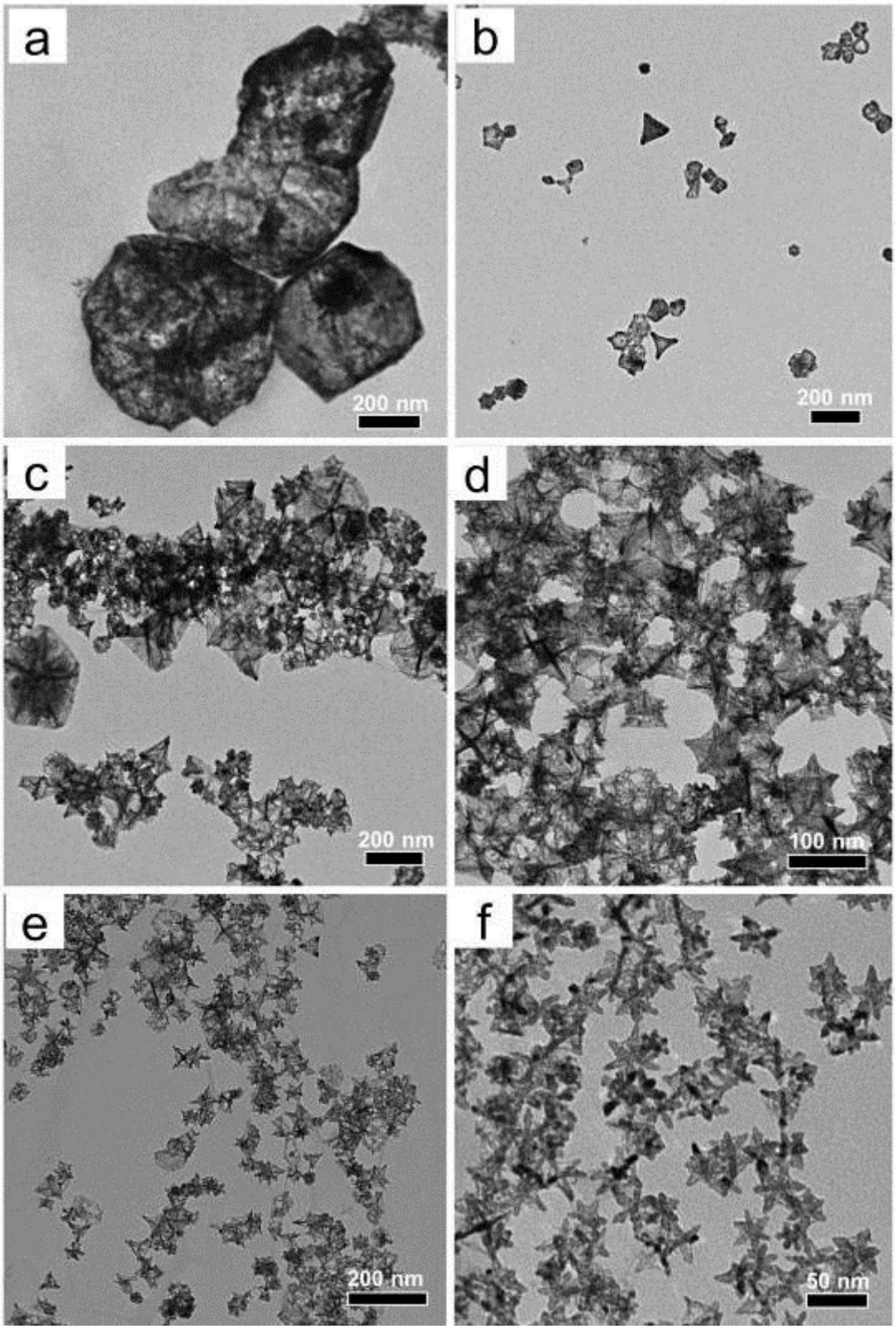

Figure S19. The TEM images of PtCuNi synthesized by the standard procedure, but with different NaI amount. (a) 0 mg, (b) 30 mg, (c) 80 mg, (d) 120 mg, (e) 150 mg, and (f) 400 mg.

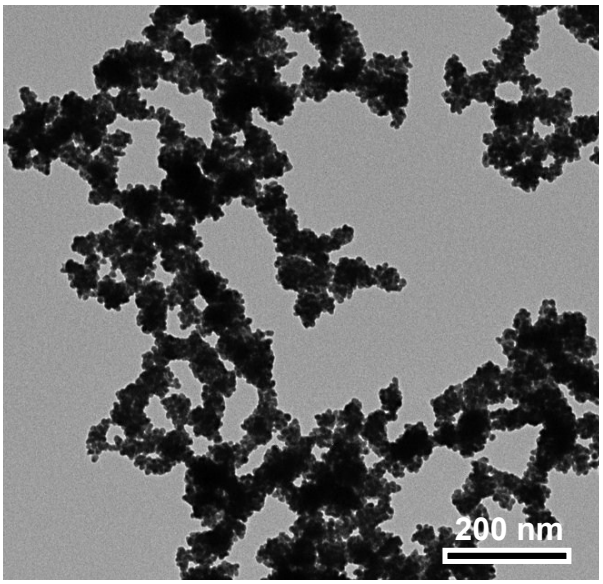

Figure S20. The TEM images of PtCuNi synthesized by the standard procedure, but change the glycine with 300 mg glutamic acid.

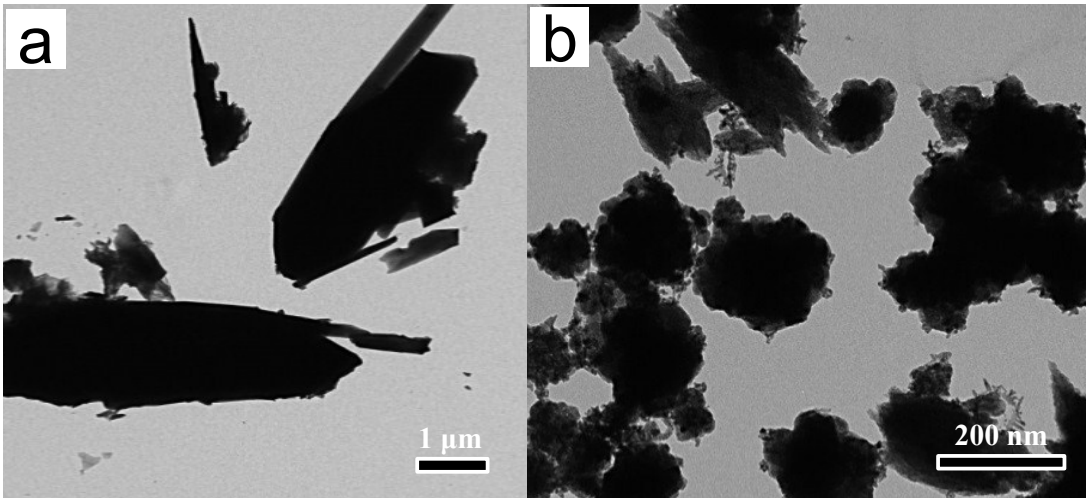

Figure S21. TEM images of PtCuNi synthesized by the standard procedure, but varying the amount of $CuCl_2$ and $NiCl_2$, (a) $CuCl_2$ 2.0 mL, $NiCl_2$ 0.2 mL, (b) $CuCl_2$ 1.6 mL, $NiCl_2$ 0.4 mL.

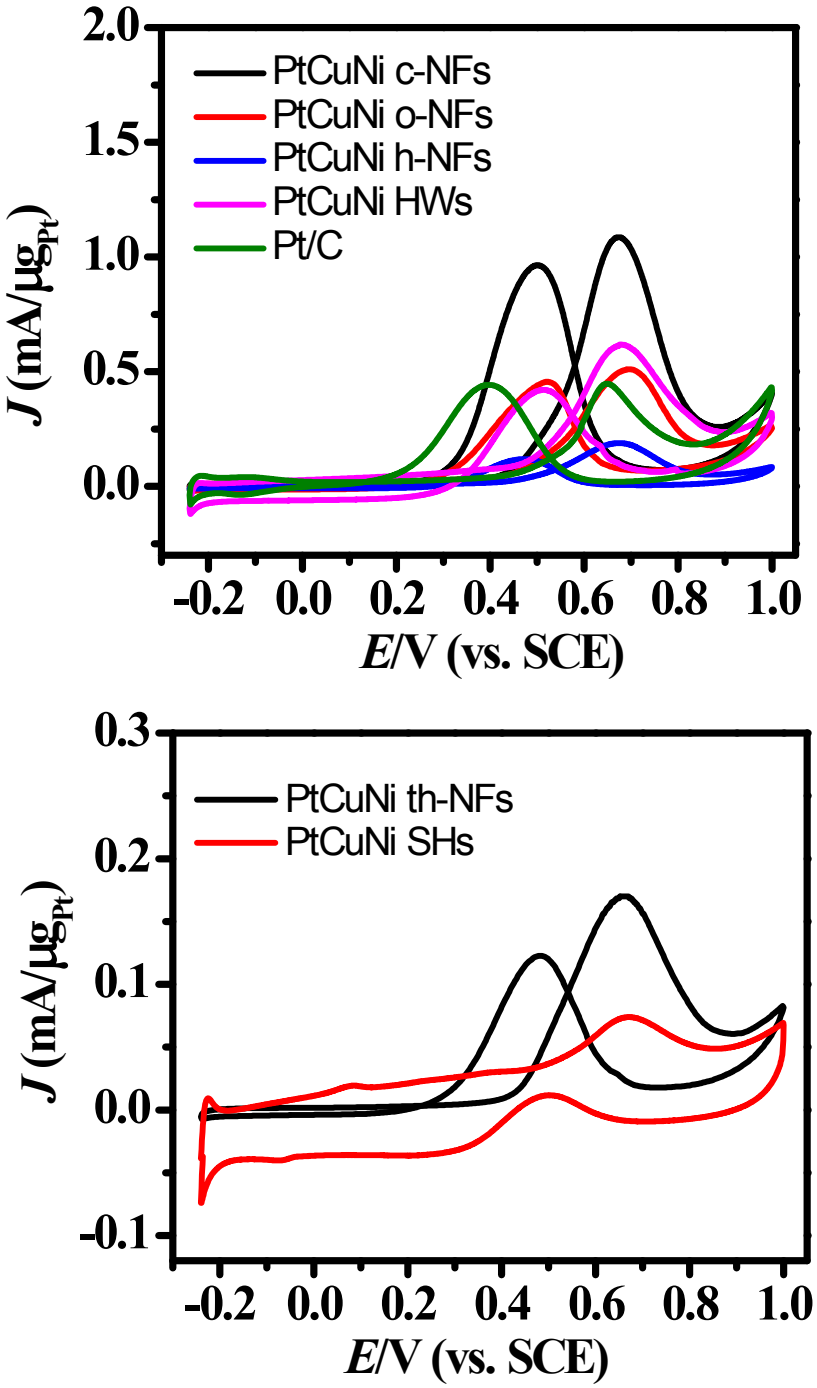

Figure S22. Cyclic voltammograms of methanol electro-oxidation for PtCuNi and Pt/C in a mixture of 0.5 M H_2SO_4 and 2 M CH_3OH at a scan rate of 50 mV/s.

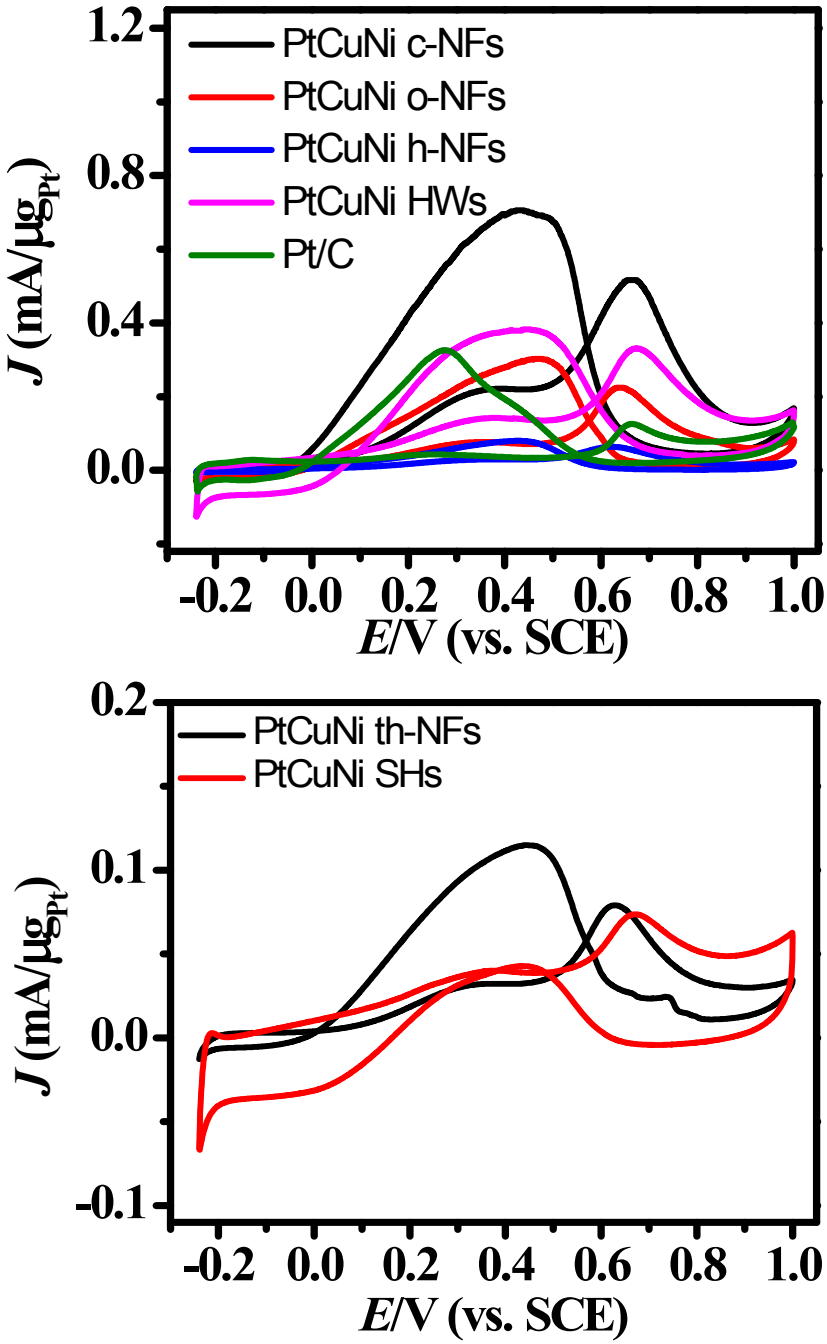

Figure S23. Cyclic voltammograms of formic acid electro-oxidation over PtCuNi and Pt/C in a mixture of 0.5 M H_2SO_4 and 0.25 M HCOOH at a scan rate of 50 mV/s.

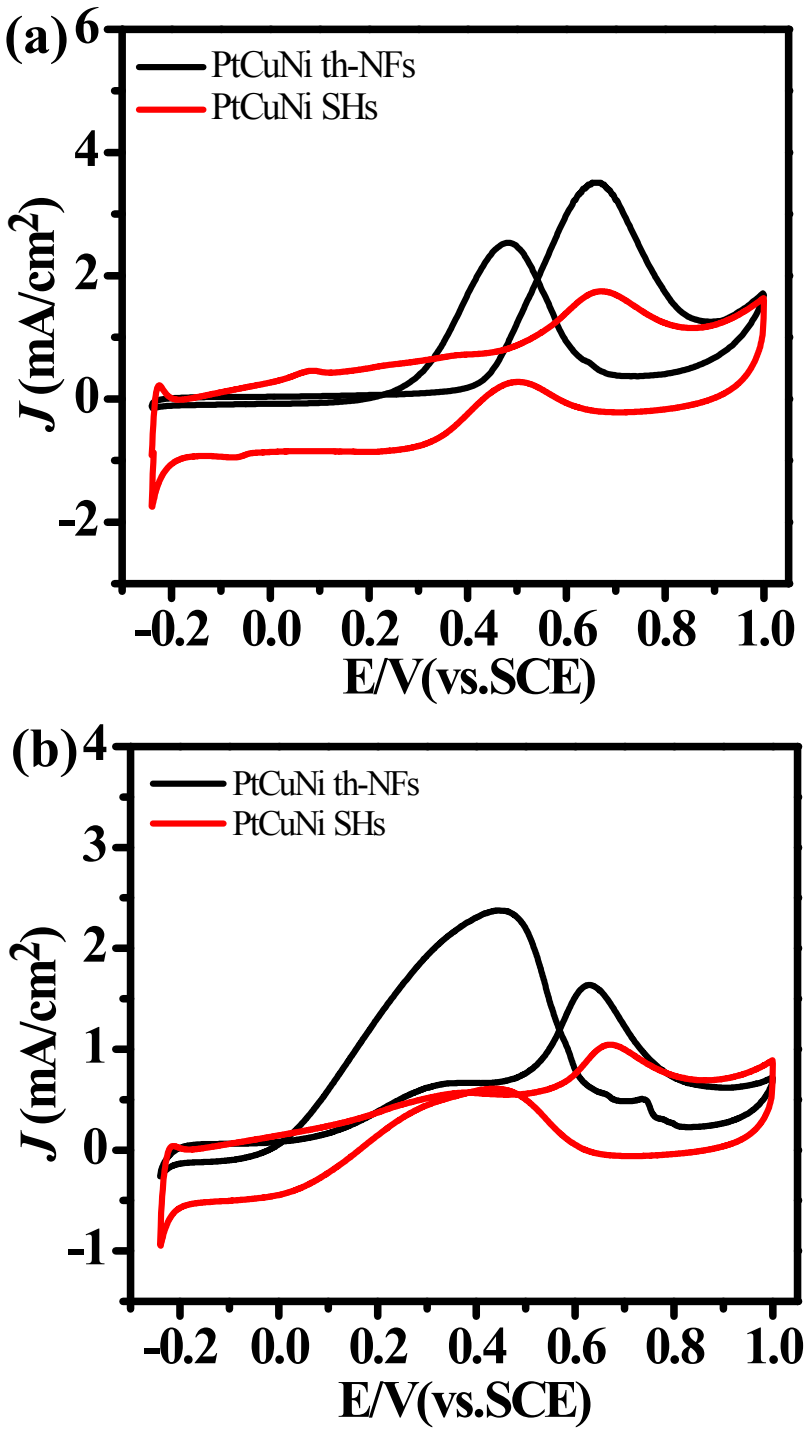

Figure S24. (a) Cyclic voltammograms of methanol electro-oxidation for th-NFs and SHs PtCuNi in a mixture of 0.5 M H_2SO_4 and 2 M CH_3OH at a scan rate of 50 mV/s. (b) Cyclic voltammograms of formic acid electro-oxidation in a mixture of 0.5 M H_2SO_4 and 0.25 M HCOOH at a scan rate of 50 mV/s.

References

[1] Luan C, Zhou Q X, Wang Y, et al. A General Strategy Assisted with Dual Reductants and Dual Protecting Agents for Preparing Pt-Based Alloys with High-Index Facets and Excellent Electrocatalytic Performance[J]. Small, 2017, 13(46), 1702617.

[2] Qi Y, Bian T, Choi S I, et al. Kinetically controlled synthesis of Pt-Cu alloy concave nanocubes with high-index facets for methanol electro-oxidation[J]. Chemical Communications, 2014, 50(5), 560-562.

[3] Xu X, Zhang X, Sun H, et al. Synthesis of Pt-Ni alloy nanocrystals with high-index facets and enhanced electrocatalytic properties[J]. Angewandte Chemie, 2014, 126(46), 12730-12735.

[4] Zhan F, Bian T, Zhao W, et al. Facile synthesis of Pd-Pt alloy concave nanocubes with high-index facets as electrocatalysts for methanol oxidation[J]. CrystEngComm, 2014, 16(12), 2411-2416.

[5] Zhang P, Dai X, Zhang X, et al. One-pot synthesis of ternary Pt-Ni-Cu nanocrystals with high catalytic performance[J]. Chemistry of Materials, 2015, 27(18), 6402-6410.

[6] Huang X, Zhao Z, Fan J, et al. Amine-assisted synthesis of concave polyhedral platinum nanocrystals having {411} high-index facets[J]. Journal of the American chemical Society, 2011, 133(13), 4718-4721.

[7] Cui Z, Chen H, Zhao M, et al. Synthesis of structurally ordered Pt_3Ti and Pt_3V nanoparticles as methanol oxidation catalysts[J]. Journal of the American chemical society, 2014, 136(29), 10206-10209.

[8] Fu G T, Xia B Y, Ma R G, et al. Trimetallic PtAgCu@ PtCu core@ shell concave nanooctahedrons with enhanced activity for formic acid oxidation reaction[J]. Nano Energy, 2015, 12, 824-832.

[9] Bu L, Guo S, Zhang X, et al. Surface engineering of hierarchical platinum-cobalt nanowires for efficient electrocatalysis[J]. Nature communications, 2016, 7, 11850.

[10] Wang L, Yamauchi Y. Metallic nanocages: synthesis of bimetallic Pt-Pd hollow nanoparticles with dendritic shells by selective chemical etching[J]. Journal of the American Chemical Society, 2013, 135(45), 16762-16765.

[11] Y. Qin, X. Zhang, X. Dai, et al. Graphene Oxide-Assisted Synthesis of Pt–Co Alloy Nanocrystals with High-Index Facets and Enhanced Electrocatalytic Properties, Small, 2016, 12, 524-533.

[12] P. Zhang, X. Dai, X. Zhang, et al. One-Pot Synthesis of Ternary Pt–Ni–Cu Nanocrystals with High Catalytic Performance, Chem. Mater., 2015, 27, 6402-6410.

[13] Du H, Luo S, Wang K, et al. High-quality and deeply excavated Pt3Co nanocubes as efficient catalysts for liquid fuel electrooxidation[J]. Chemistry of Materials, 2017, 29(22), 9613-9617.

[14] Luo M, Sun Y, Zhang X, et al. Stable High-Index Faceted Pt Skin on Zigzag-Like PtFe Nanowires Enhances Oxygen Reduction Catalysis[J]. Advanced Materials, 2018, 30(10), 1705515.

[15] Ding J, Bu L, Guo S, et al. Morphology and phase controlled construction of Pt–Ni nanostructures for efficient electrocatalysis[J]. Nano Letters, 2016, 16(4), 2762-2767.

[16] Xue S, Deng W, Yang F, et al. Hexapod PtRuCu Nanocrystalline Alloy for Highly Efficient and Stable Methanol Oxidation[J]. ACS Catalysis, 2018, 8(8), 7578-7584.

[17] Zhang N, Bu L, Guo S, et al. Screw thread-like platinum–copper nanowires bounded with high-index facets for efficient electrocatalysis[J]. Nano Letters, 2016, 16(8), 5037-5043.

[18] Huang L, Zhang X, Han Y, et al. High-index facets bounded platinum–lead concave nanocubes with enhanced electrocatalytic properties[J]. Chemistry of Materials, 2017, 29(10), 4557-4562.

[19] Xu X, Zhang X, Sun H, et al. Synthesis of Pt–Ni Alloy Nanocrystals with High-Index Facets and Enhanced Electrocatalytic Properties[J]. Angewandte Chemie, 2014, 126(46), 12730-12735.

[20] Luo S, Shen P K. Concave platinum–copper octopod nanoframes bounded with multiple high-index facets for efficient electrooxidation catalysis[J]. ACS nano, 2016, 11(12), 11946-11953.

[21] Kuang Y, Cai Z, Zhang Y, et al. Ultrathin dendritic Pt_3Cu triangular pyramid caps with enhanced electrocatalytic activity[J]. ACS applied materials & interfaces, 2014, 6(20), 17748-17752.

[22] Huang L, Zhang X, Wang Q, et al. Shape-control of Pt–Ru nanocrystals: tuning surface structure for enhanced electrocatalytic methanol oxidation[J]. Journal of the American Chemical Society, 2018, 140(3), 1142-1147.

[23] Tang M, Luo S, Wang K, et al. Simultaneous formation of trimetallic Pt-Ni-Cu excavated rhombic dodecahedrons with enhanced catalytic performance for the methanol oxidation reaction[J]. Nano Research, 2018, 11(9), 4786-4795.